



Experimental Study on Strain Burst Characteristics of Sandstone Under True Triaxial Loading and Double Faces Unloading in One Direction

Manchao He¹ · Fuqiang Ren² · Dongqiao Liu¹ · Shudong Zhang¹

Received: 9 January 2019 / Accepted: 5 October 2020 / Published online: 27 October 2020
© Springer-Verlag GmbH Austria, part of Springer Nature 2020

Abstract

In this study, a new strain burst test system was used to conduct two types of strain burst experiments by rapidly unloading single and double faces (in one direction), to simulate the strain burst occurring in surrounding rock of tunnel or double tunnel faces during the opposite tunneling. A high-speed image recording system and an acoustic emission system were used to monitor the failure process of strain burst of red sandstone. The commonalities of these two types of strain burst are as follows: failure stress and percentage of dissipation energy due to crack propagation were approximately equal; the evolution of mean velocity of free face was similar, which suddenly increased first and then decreased, then the gradient increased to the extremum value, and finally decreased to zero. Subregions of the fracture were consistent, and both showed shear, buckling, splitting, and ejection zones. However, the strain burst intensity for unloading double faces was larger than that for unloading single face, as demonstrated by a larger initial ejection velocity, larger volume of burst pit, and lower peak frequency. Furthermore, when double faces were unloaded, the flaky and massive features of fragments obtained due to strain burst were more obvious than the fragments obtained from the unloading of single face. Moreover, from yield to burst, when double faces were unloaded, the sandstone strain burst contained more shear microcracks, whereas the strain burst when unloading single face contained more tensile microcracks.

Keywords Strain burst · Unloading double faces · Ejection velocity field · Fracture subregions · Peak frequency

List of Symbols

$\sigma_{10}, \sigma_{20}, \sigma_{30}$	Initial maximum, intermediate, minimal principal stress, respectively
$\sigma_H, \sigma_h, \sigma_v$	Two horizontal and a vertical in situ stresses
σ_{X1}, σ_{X2}	Minimal principal stress in negative and positive X -directions, respectively
U	Total strain energy
U_e	Elastic strain energy
U_k	Kinetic energy
U_d	Dissipation energy
U_e^r	Releasable elastic strain energy
U_d^p	Dissipation energy due to plastic deformation before yield
U_d^1	Dissipation energy due to crack propagation from yield to burst

U_d^2	Dissipation energy due to crack propagation during burst process
v	Ejection velocity
v_y, v_z	Horizontal and vertical ejection velocity
v_{max}	Maximum initial ejection velocity
m	Total mass of ejection fragments
d, d_1, d_2	Maximum distance between buckling cracks and free face
l, w, h	Length, width and thickness of fragments
RA	Rise time divide by amplitude

1 Introduction

Rock bursts commonly occur along deep mine roadways under high geostress. Rock bursts can be classified into the following three types: fault slip burst, pillar burst, and strain burst (Kaiser et al. 1996). Strain bursts are self-initiated rock burst, corresponding to the response of strain energy accumulation and release induced by the excavation of surrounding rock (Ortlepp and Stacey 1994). Strain bursts pose a serious threat to the safe excavation

✉ Fuqiang Ren
renfuqiangcumtb@163.com

¹ State Key Laboratory for Geomechanics and Deep Underground Engineering, Beijing 100083, China

² School of Civil Engineering, University of Science and Technology Liaoning, Anshan 114051, China

of underground engineering. On the one hand, the strain burst significantly increases with the increase in excavation depth. For example, strain bursts have caused serious casualties many times at Jinping II hydropower station (at excavation depth of about 3000 m) in China (Chen et al. 2015). On the other hand, the complexity of underground space structure leads to the changes in the boundary conditions of typical geological units, making it difficult to prevent and control the occurrence of strain bursts.

Noteworthy, conventional studies on strain burst mechanisms are based on static rock mechanics. The balance and release of energy during a strain burst have been investigated using the energy theory (Salamon 1984; Miao et al. 2016), the fracture failure theory (Nemat-Nasser and Horii 1982; Mansurov 2001), and the damage theory (Chang and Lee 2004). The responses to stress redistribution such as crack propagation and strain energy accumulation and release induced by the excavation of surrounding rock have been considered to be the essential mechanisms for the initiation of strain burst.

In recent years, laboratory tests have been significantly promoted to better understand the concept of strain burst; and the mechanisms of damage, splitting, and ejection have been clearly explained by conducting true triaxial strain burst experiments (He et al. 2010). Furthermore, many factors influencing strain burst, such as lithology (He et al. 2012a), bedding orientation (He et al. 2012b), stiffness (He et al. 2018), loading path (Si and Gong, 2020; Ren et al. 2020), temperature (Su et al. 2017a; Akdag et al. 2018), intermediate principal stress (Su et al. 2017b), and radial stress gradient (Su et al. 2017c) have also been studied. Moreover, in the abovementioned laboratory tests, the strain burst at the surrounding rock of roadway or tunnel

with single free face was simulated by true triaxial loading and unloading single face.

However, as shown in Fig. 1, in some engineering cases, such as the cross point (Cai and Kaiser 2018) or pillar (Plessis et al. 2014) of a roadway, or the rock mass between two adjacent tunnels (Li et al. 2013), the typical geological element has double free faces. Moreover, to shorten the construction period, the tunnels are often excavated simultaneously through entrance and exit. In particular, for the double tunnel faces during the opposite tunneling, the double free faces are exposed simultaneously. Furthermore, there are three free faces of the working face of coal mine (He et al. 2012a, b, c) and four free faces of the pillar obtained after room-pillar mining (Tesarik et al. 2009). Therefore, it is necessary to carry out different types of tests to evaluate strain burst occurring in different positions.

In this study, a new strain burst test system was used to conduct two types of strain burst experiments by rapidly unloading single or double faces in one direction, to simulate the strain burst occurring in the surrounding rock of tunnel or double tunnel faces during the opposite tunneling. Additionally, the commonalities and differences of these two types of strain burst tests were analyzed from the following five aspects: failure stress, strain energy dissipation, ejection velocity field, failure mode, and acoustic emission (AE) characteristics.

2 Experimental Procedures

2.1 Sandstone Samples

The sandstone samples used herein were collected from Langfang, Hebei province, North China. X-ray diffraction



Fig. 1 Photographs of **a** rock burst at the cross point of roadway of Kidd Creek mine (Cai and Kaiser 2018) and **b** crush pillar of Lonmin (Plessis et al. 2014)

(XRD) analysis was performed on these sandstone samples. The major minerals in the sandstone samples are quartz (58.0%), dolomite (13.4%), plagioclase (6.6%), calcite (6.5%), and clay minerals (12.1%, mainly illite).

Three cylindrical specimens of sandstone with nominal dimensions of 50 mm in diameter and 100 mm in length were prepared for uniaxial compression tests. The test results are presented in Table 1. The mean value of uniaxial compression strength was 41.7 MPa. Moreover, Table 1 also presents the P-wave and S-wave velocities of sandstone; specifically, the mean P-wave velocity was ~ 3073 m s⁻¹. The tensile strength, Young’s modulus, and Poisson’s ratio were 4.21 MPa, 6.82 GPa, and 0.26, respectively.

Figure 2 shows the polarized microscope photographs of thin section (Fig. 2a) and microscale structure (Fig. 2b) of a sandstone sample. Figure 2a exhibits that the contacts between quartz and feldspar are point to point; and the gaps are filled with calcite and dolomite. The diameters of void range from 0.06 to 0.25 mm (Fig. 2b).

2.2 New Strain Burst Test System

A new true triaxial strain burst test system was used for the tests. Figure 3a shows the photograph of experimental machine and Table 2 lists the specifications of new system. Based on the last generation system (He et al. 2010), this new generation strain burst machine incorporates the

following improvements: the maximum loading capacity is increased by more than ten times (450–5000 kN in vertical direction) compared to the old system; and the horizontal loading capacity is increased by more than four times (450–2000 kN in both horizontal directions). The stiffness of frame is also increased from 1.2 to 10 GN m⁻¹. The most important improvement involves the capacity of unloading: The old system rapidly unloads only single face, whereas the new machine can unload double, triple, and four faces, thus simulating the strain burst of different positions. Moreover, the new system uses a hydraulic servo-control for loading, and the loading rate ranges from 10 N/s to 10 kN s⁻¹.

A displacement sensor was installed on the front side of piston, as shown in Fig. 3b. The measured deformation includes three parts: loading rod, rigid plate, and rock sample. Moreover, the stiffness of loading rod is ~ 4 GN m⁻¹, and the rigidity of plate is ~ 400 GPa. Therefore, the rigidities of loading rod and plate are larger than that of rock sample (less than 80 GPa), i.e., the deformations of loading rod and plate are far less than that of the rock sample. Therefore, the measured deformation can be used to calculate strain of sample.

The sample shape was cubic and three kinds of side lengths (100, 150, or 300 mm) were provided. In this study, the sandstone blocks were machined into cubic specimens with an approximate side length of 150 mm, unlike the previous studies typically conducted on cuboid prisms with dimensions of 150 mm × 60 mm × 30 mm (He et al. 2010) or

Table 1 Physical and mechanical properties of the sandstone

Density (g/cm ³)	Mineral components (%)			P-wave velocity (m/s)	S-wave velocity (m/s)	UCS (MPa)	Tensile strength (MPa)	Young’s modulus (GPa)	Poisson’s ratio
	Quartz	Dolomite	Clay						
2.26	58.0	13.4	12.1	3073	1776	41.7	4.21	6.82	0.26

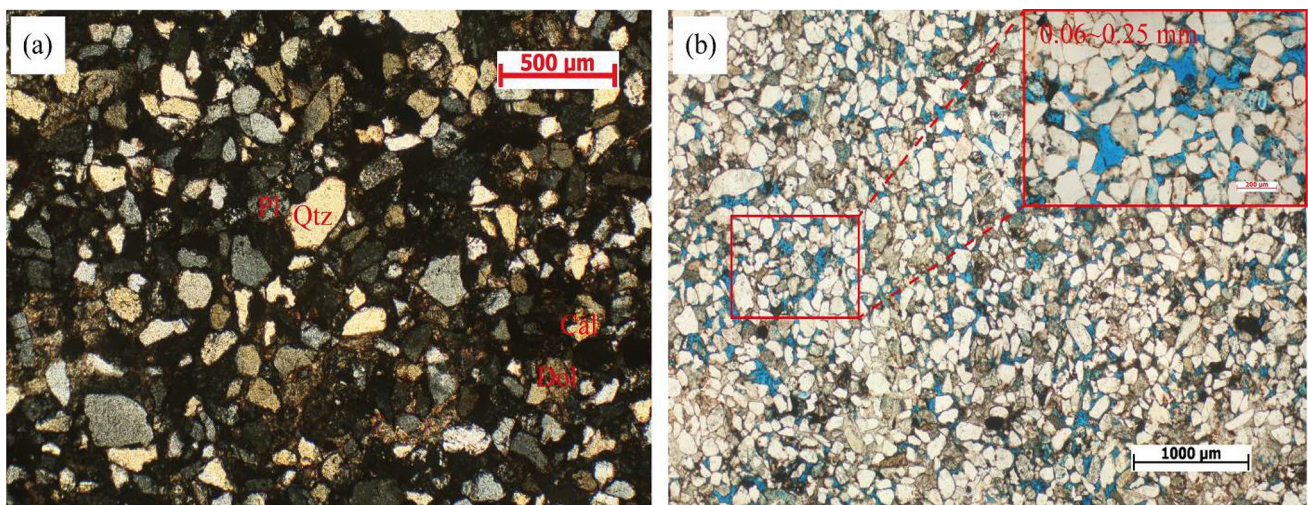


Fig. 2 Polarized microscope photographs of the sandstone samples; **a** relationship of mineral combination and **b** microscopic void structure

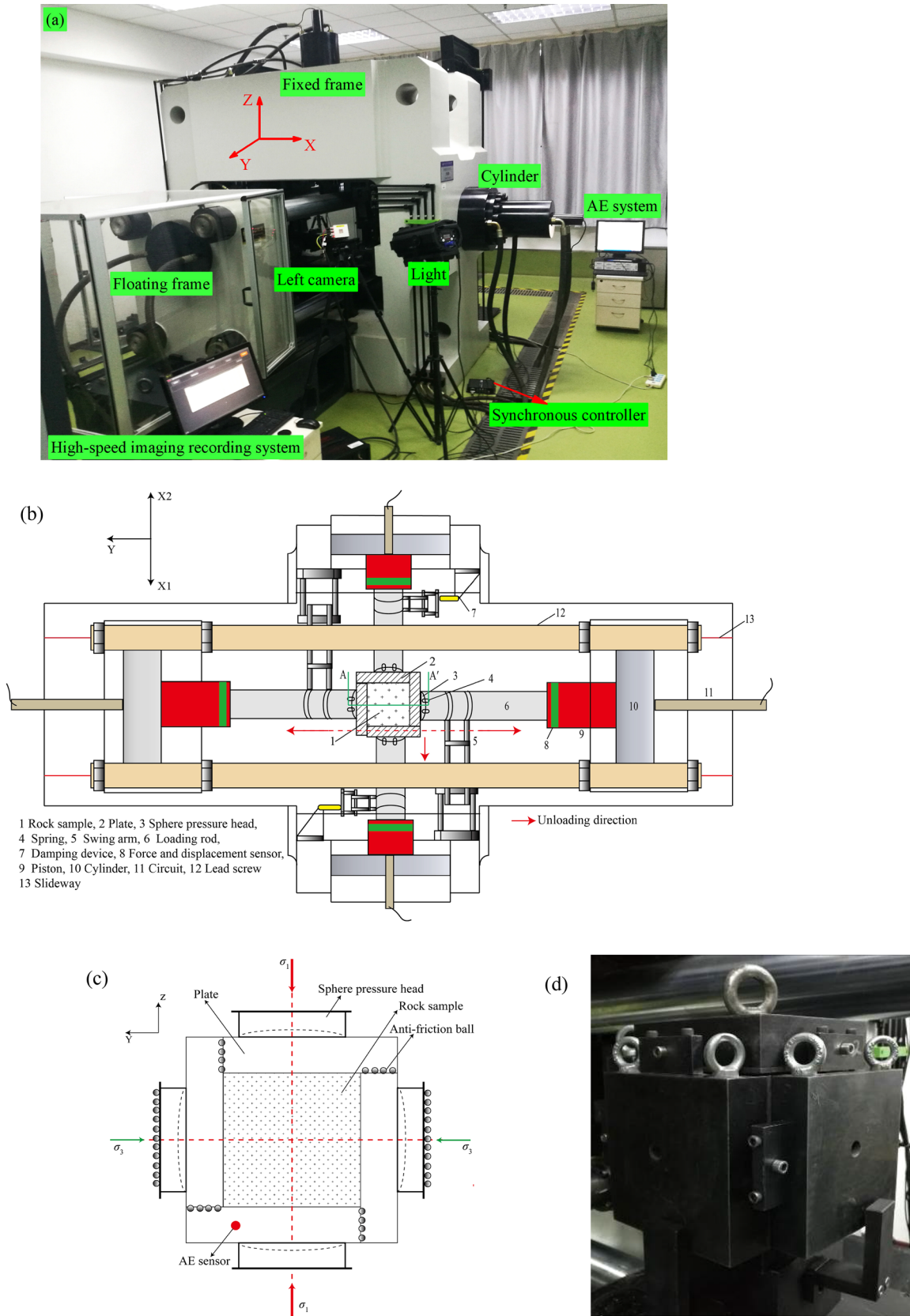


Fig. 3 Experimental system; **a** main machine; **b** schematic of profile of main machine in the *xoy* plane; **c** schematic of working principle (After Alexeev et al. 2004; Feng et al. 2018) and **d** photograph of the

sample box; top view of the high-speed camera positions for unloading **e** single face and **f** double faces tests

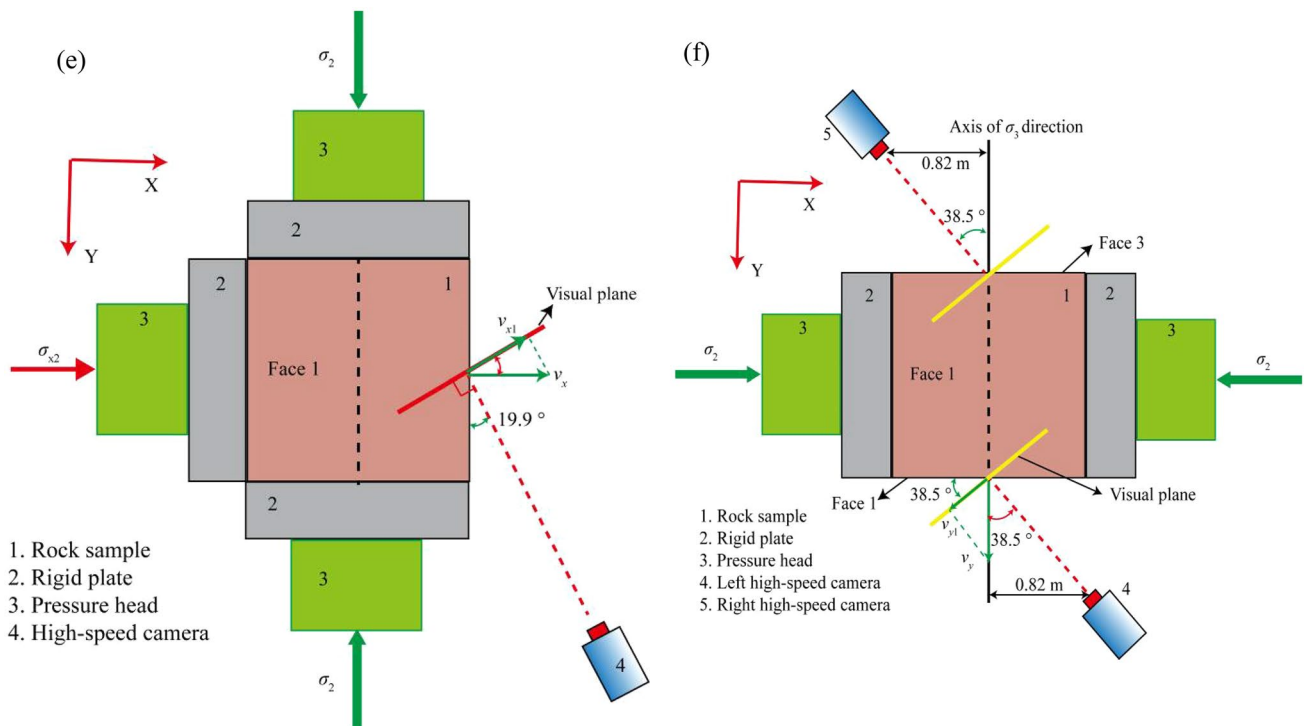


Fig. 3 (continued)

Table 2 Specifications of the new true triaxial strain burst instrument

Standard specimen size (mm)	Maximum specimen size (mm)	X-, Y-direction maximum load (kN)	Z-direction maximum load (kN)	Control	Loading rate (kN/s)	Unloading capacity
150×150×150	300×300×300	2000	5000	Hydraulic servo-control	0.01–10	Unloading 1–4 faces rapidly ^a

^aThe single, double, triple and four faces can be unloading rapidly

200 mm × 100 mm × 100 mm (Su et al. 2017a). Importantly, a larger thickness makes the fracture zone clearer. Furthermore, six rigid loading plates were used in the mutual sample box. Figure 3c, d shows the working principle (Alexeev et al. 2004; Feng et al. 2018) and photograph of sample box used herein. The loading plate completely covered the surface of rock sample and moved with sample deformation. Antifriction balls were installed in the interfaces of plates to reduce the friction between plates. Moreover, a spherical pressure head was installed on the head of loading rod to adjust the rock sample and create a level face.

When single face was unloaded, the loading in positive X-direction (X1, Fig. 3b) was removed to expose single free face. When double faces were unloaded simultaneously, the loadings in the positive and negative y-directions were synchronously removed. First, the hydraulic cylinder piston retreated quickly, the swing arm (element 5, Fig. 3b) rapidly dropped under the action of assistant device, and the loading

plate was then separated from the specimen under the action of spring. Finally, the plate fell due to gravity and to expose the double free faces. The amount of time taken from removing force to the exposure of free face was about 365 ms. When the swing arm fell, a damping device absorbed the kinetic energy of swing arm to maintain its stability.

2.3 Monitoring System

The monitoring system was equipped with an AE system and a high-speed image recording system. Figure 3a shows that a Micro-II system produced by the American Physical Acoustics Corporation was used for AE monitoring. This system uses an 18-bit A/D switching technology that allows instantaneous time–waveform recording. In this study, the AE signals were amplified to 100 times (amplifier was set as 40 dB); and the threshold, sampling frequency, and sampling length were set as 40 dB, 5 MHz, and 4096 data points,

respectively. A Nano-30 sensor with a response frequency of 100–400 kHz was used to acquire the AE signals. The sensor was glued to the bottom plate as shown in Fig. 3c.

Furthermore, the binocular high-speed photograph system was equipped with two high-speed cameras connected with a synchronous controller (Fig. 3a); and each camera was connected to the corresponding collector and memory with cables (the maximum data transfer rate was 25 Gbit s^{-1}). The two cameras were able to synchronously and accurately capture images. Figure 3e, f shows the diagram of position of high-speed cameras, respectively, for unloading single and double faces.

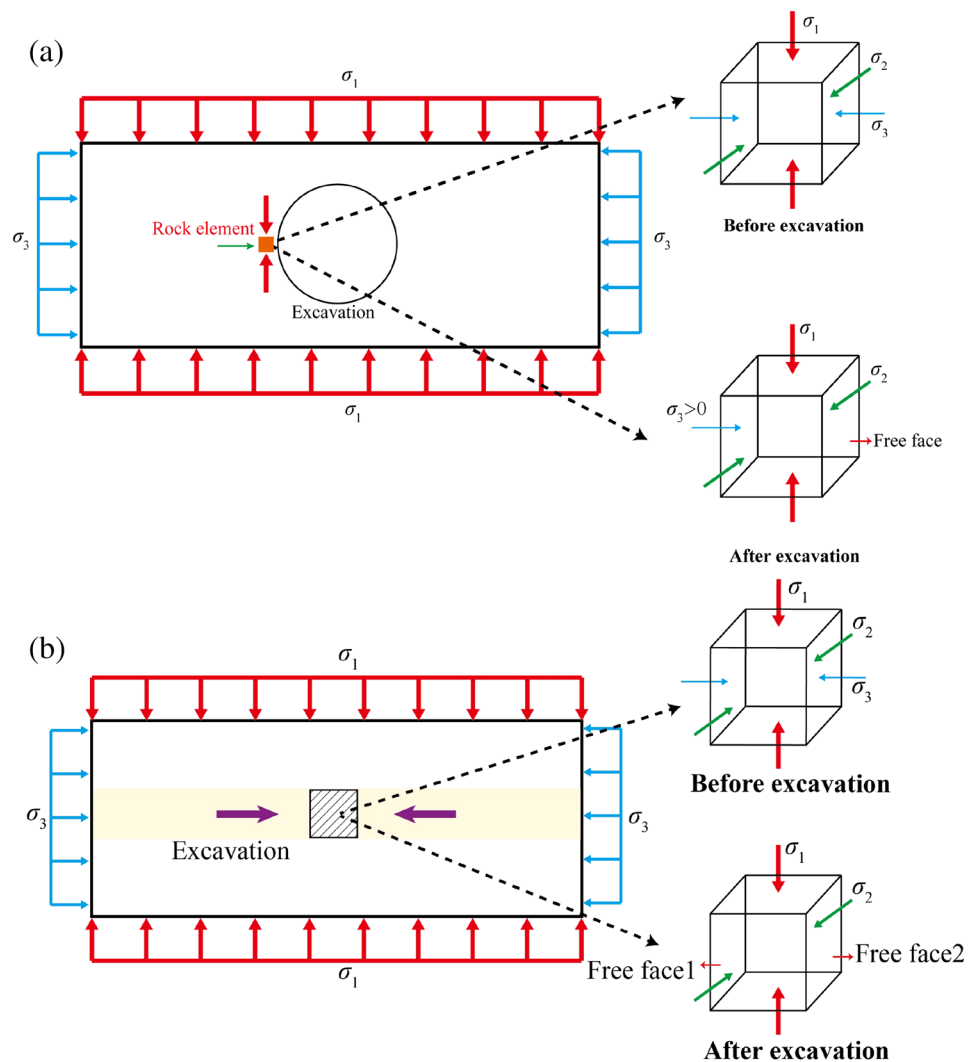
2.4 Experimental Scheme

Two types of strain burst tests were conducted in this study. The first test simulated the strain burst that occurs in the side of a tunnel; and the second test simulated the strain burst that occurs in double tunnel faces during the

opposite tunneling. Figure 4 shows the stress transformation during the abovementioned two types of strain burst tests. For the former test (Fig. 4a), the rock element was under a state of three directions compression before excavation. However, after excavation, the rock element formed a free face; and the stress in the opposite face was still greater than zero. For the second strain burst test (Fig. 4b), the rock mass between tunnel faces was also under a state of three directions compression before excavation, while double free faces were exposed due to the simultaneous opposite excavation of tunnel. Figure 3b demonstrates that the two cylinders in X -direction are independent; during the loading, the piston in X_2 direction was set as a fixed end. However, when σ_{X_1} was unloaded, σ_{X_2} increased to 1.0 MPa and remained constant.

Therefore, two types of loading paths were designed to simulate the abovementioned two types of strain burst. Figure 5a shows the loading path of former strain burst. The initial stress state was identified according to the fitted general

Fig. 4 Schematic of stress transformation process of the rock element when unloading **a** single and **b** double faces



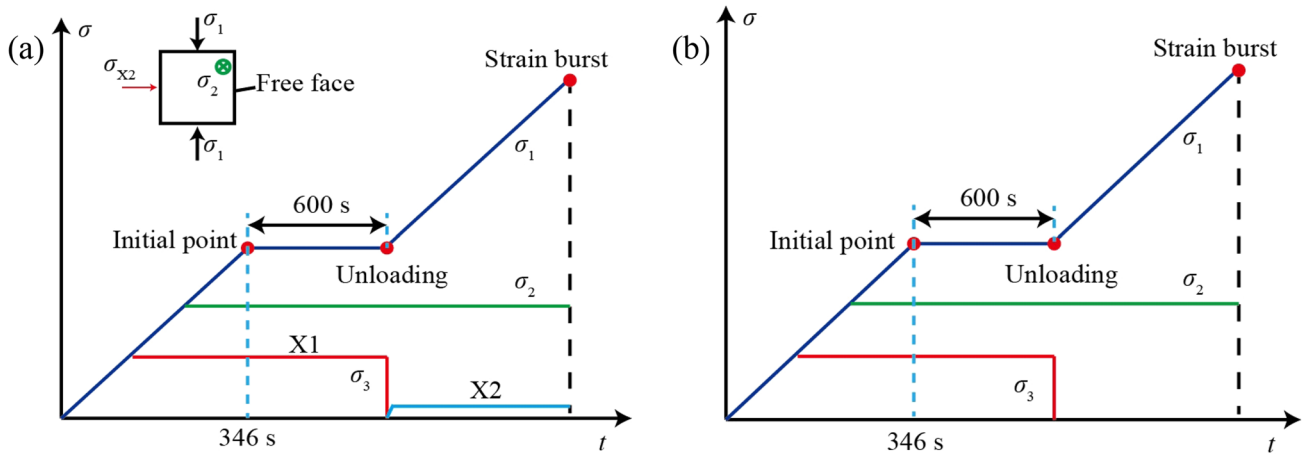


Fig. 5 Loading paths of two types of strain burst tests: unloading **a** single and **b** double faces

far-field stress relationship at depth for North China by Sun and Tan (1995), as shown in Eq. (1):

$$\begin{aligned}
 \sigma_H &= 0.02930H + 1.3548, \\
 \sigma_h &= 0.01801H + 1.0018, \\
 \sigma_v &= 0.02532H + 0.4177,
 \end{aligned}
 \tag{1}$$

where σ_H , σ_h , and σ_v are two horizontal and one vertical in situ stresses, respectively, and H denotes the depth. For a sandstone present 1000 m below the surface, the initial stresses are approximately $\sigma_{10} = 30.8$ MPa, $\sigma_{20} = 25.7$ MPa, and $\sigma_{30} = 19.0$ MPa. During the loading in the X1 direction, the displacement in the X2 direction was kept constant. When the stress arrived at the initial point, the three directions stresses were maintained for about 10 minutes to create a uniform stress distribution. The minimal principal stress in X1 direction was then unloaded to simulate excavation, while maintaining a constant stress ($\sigma_{X2} = 1.0$ MPa) in the X2 direction. Finally, the maximum principal stress was increased by 2 kN s^{-1} ($\sim 0.1 \text{ MPa s}^{-1}$) until strain burst, while maintaining σ_2 to be constant.

The loading path of second strain burst (unloading of double faces, Fig. 5b) was similar to the first test simulation; however, when the initial state was maintained for a period, the minimal principal stress in the Y-direction (double faces) was rapidly unloaded to simulate the opposite excavation of the tunnel. Finally, the maximum principal stress was increased by 2 kN s^{-1} until strain burst.

3 Results and discussion

3.1 Failure Stress

Figure 6 shows the stress–strain curves of the abovementioned two types of strain burst (Fig. 6a, b for unloading of single and double faces, respectively). Table 3 presents the corresponding failure stress for the two types of strain burst tests. A clear yield point was observed; the yield stresses were 100.9 and 101.2 MPa for the unloading of single and double faces, respectively. The yield stresses of the above two kinds of tests were close because the rock failure is mainly controlled by the $(\sigma_1 - \sigma_3)$ when the intermediate principal stress was unconsidered. Additionally, when single face was unloaded, the strain (12.4%) of yield point was smaller than the strain (14.3%) when unloading double faces. The maximum principal strain exhibited the same trend as the yield point strain. For the abovementioned two types of strain burst, the time intervals from yield to burst were very short, about 8.6 and 6.3 s, respectively.

As shown in Fig. 7a, the sample expands laterally along the X-direction owing to the Poisson effect during the axial stress concentration after unloading. However, in the X2 direction, the restraining stress restricts the lateral deformation to a certain extent, and the lateral expansion is generally in the direction of free surface. Therefore, the lateral friction of surface in the direction of intermediate principal stress (Y-direction) is τ_{yx} , and the direction is away from the free surface. Similarly, Fig. 7b demonstrates the deformation of

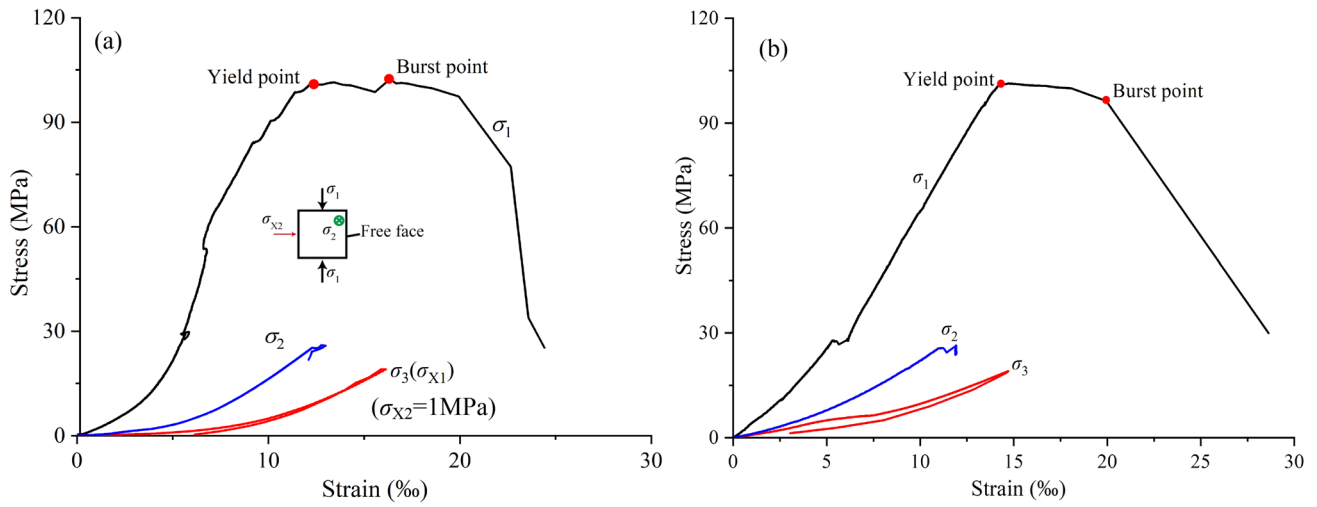


Fig. 6 Stress–strain curves of the two types of strain burst tests: unloading **a** single and **b** double faces

Table 3 Failure stress of the two types of strain burst

Type	Initial stress (MPa)	σ_1 of yield (MPa)	Strain burst stress (MPa)	ϵ_1 of yield (%)	Maximum ϵ_1 (%)
Unloading single face	$\sigma_{10} = 30.8$ $\sigma_{20} = 25.7$	100.9	$\sigma_1 = 101.9, \sigma_2 = 28.7$ $\sigma_3(\sigma_{X1}) = 0.0, \sigma_{X2} = 0.8$	12.4	24.4
Unloading double faces	$\sigma_{30} = 19.0$	101.2	$\sigma_1 = 96.7, \sigma_2 = 26.2$ $\sigma_3 = 0.0$	14.3	28.6

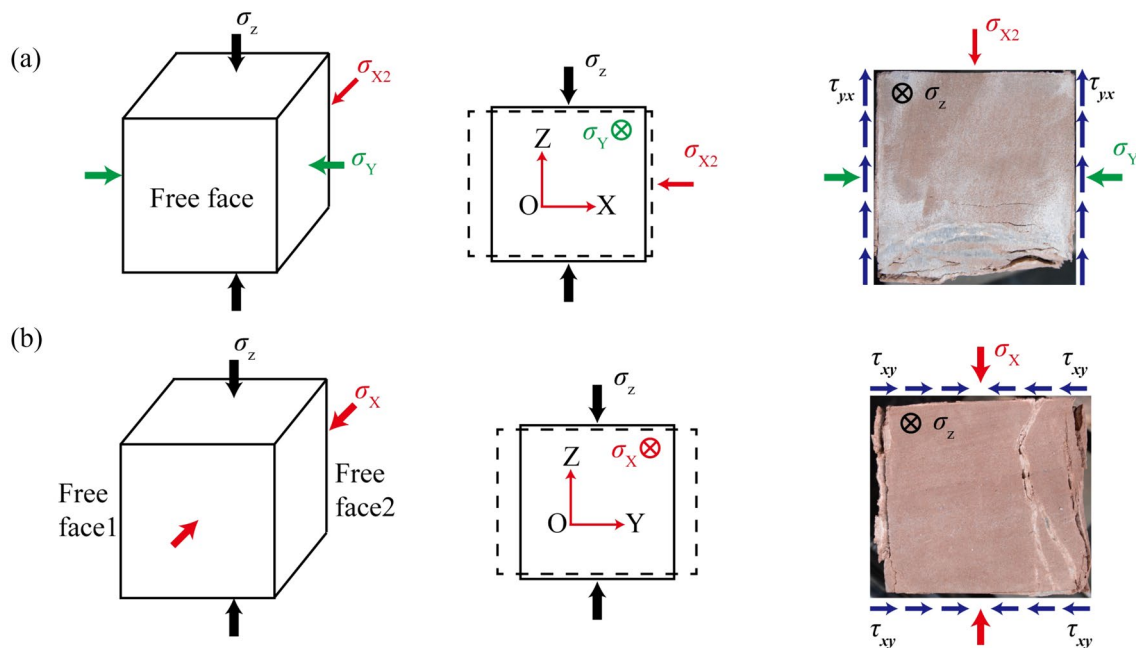


Fig. 7 Diagram of deformation mechanism of strain burst samples: unloading **a** single and **b** double faces

specimen during the maximum principal stress concentration after unloading double faces, the expansion deformations at the two free faces are basically the same; nonetheless, the directions are opposite. Therefore, the lateral friction on the surfaces of intermediate principal stress (*X*-direction) cancels out each other. Moreover, owing to the heterogeneity of rock, the actual deformation at the two free faces is not exactly the same; and the lateral friction is much smaller than the strain burst experiment with single free face. In fact, the constraint on ejection failure can also be reduced when unloading double faces. Therefore, under the same conditions, the strain burst when unloading double faces is more intense than that when unloading one free face.

3.2 Analysis of Dissipation Energy

The total strain energy (*U*) can be divided into two sections [as expressed in Eq. (1)]; elastic strain energy (*U_e*) and dissipation energy (*U_d*) (Huang and Li 2014). Similarly, the elastic strain energy (*U_e*) also contains two sections (Eq. (2)): releasable (*U_e^r*) and residual (*U_e^r*) elastic strain energy. Furthermore, the dissipation energy is responsible for crack propagation and plastic deformation in rock samples and can be expressed as Eq. (3). Figure 8a shows the schematic illustration of strain energy calculation, where *U_d^p* represents the strain energy consumed by plastic deformation before yield. *U_d¹* represents the strain energy consumed by crack propagation from yield to burst, while *U_d²* is the energy consumed during burst.

$$U = U_e + U_d, \tag{2}$$

$$U_e = U_e^r + U_r, \tag{3}$$

$$U_d = U_d^1 + U_d^2 + U_d^p. \tag{4}$$

Figure 8b, c shows the five parts of strain energy in the maximum principal stress direction for the unloading of single and double faces tests, respectively. The slope of boundary line (blue line) was determined from the slope of stress–strain curve in the elastic stage. The areas of the five sections show the strain energy density of rock sample. Table 4 summarizes the specific values of total energy density and the percentages of five parts of strain energy in total. The values of total strain energy of the two types of strain burst were closed, and the percentages of strain energy consumed during crack propagation were also approximately equal (62.5 and 63.3%, respectively, for the unloading of single and double faces). For unloading single face, the energy consumed by plastic deformation was greater than that when unloading double faces. Furthermore, more strain energy was consumed from yield to burst for unloading double

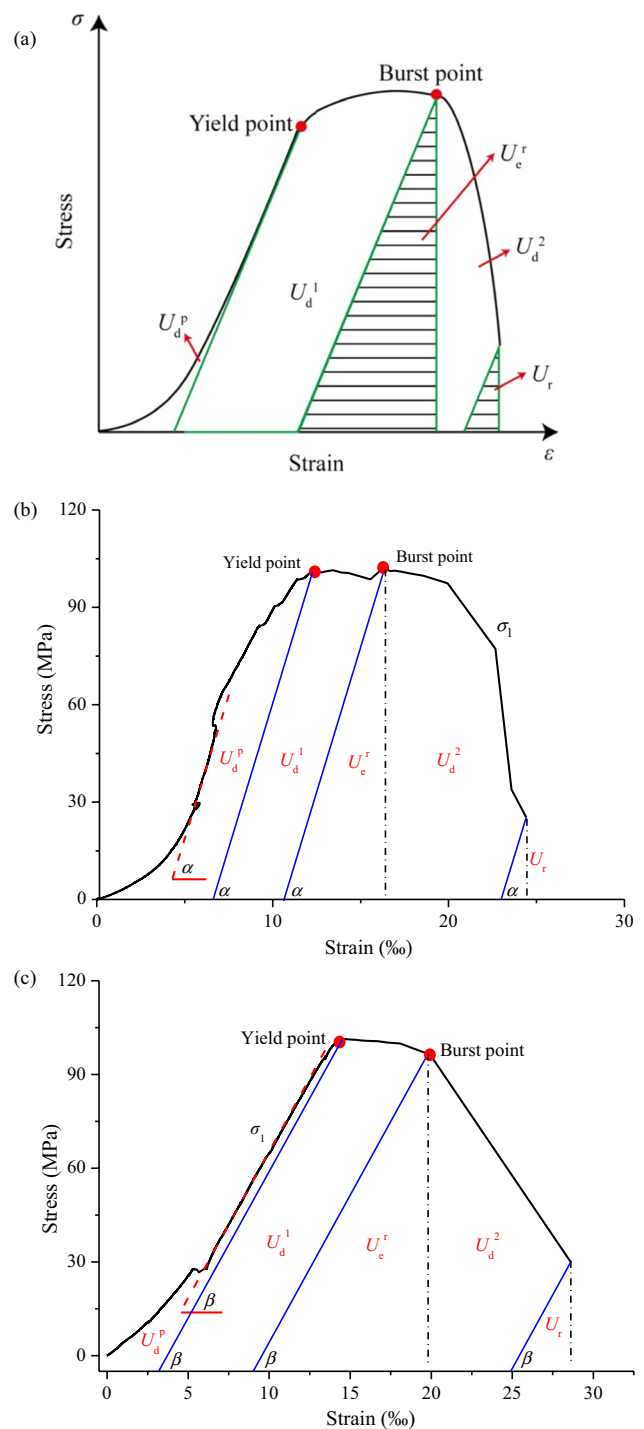
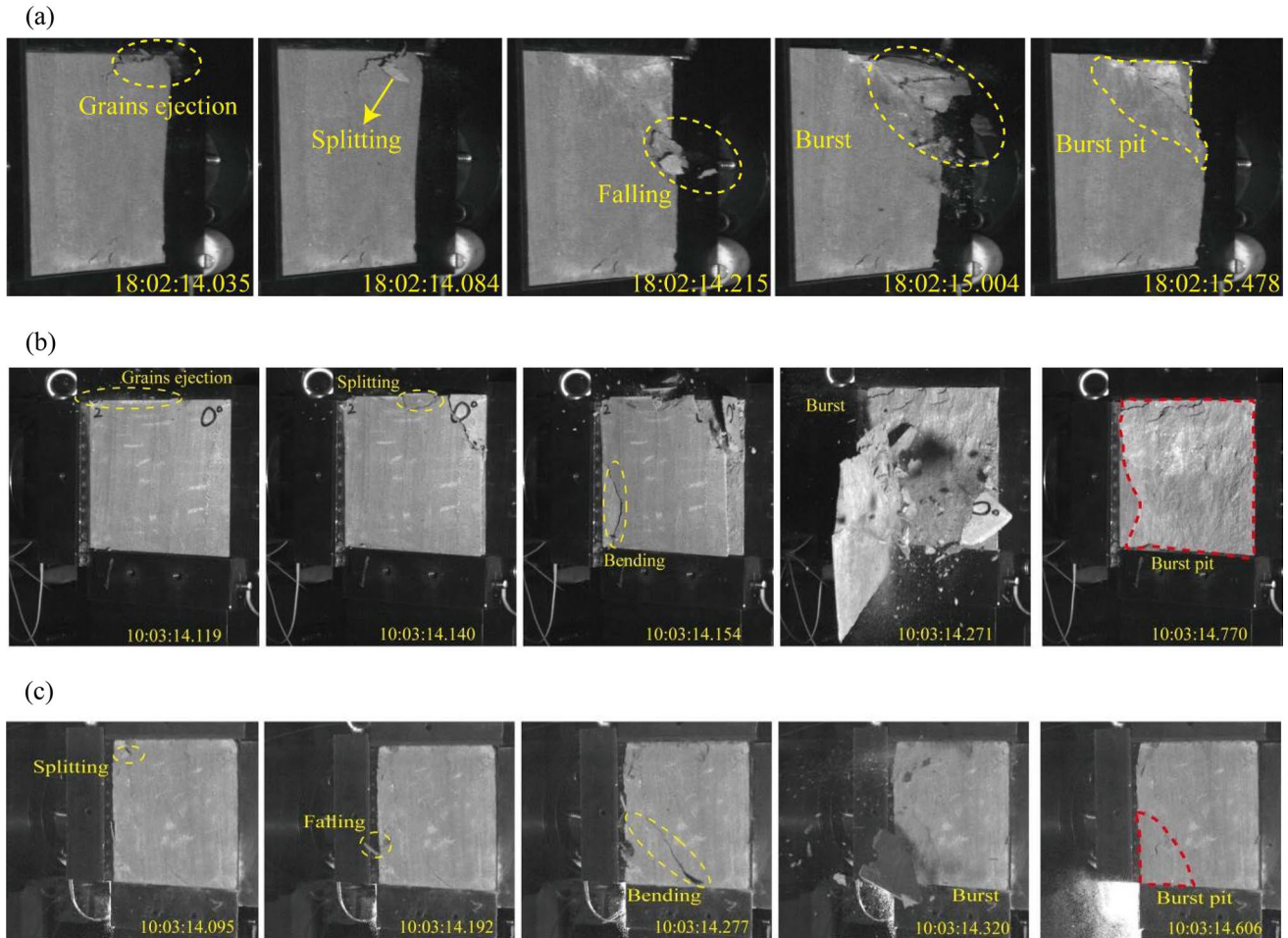


Fig. 8 a Schematic of the strain energy calculation; the specific calculation process of the strain burst tests for unloading b single and c double faces

faces, whereas the energy consumed during the burst stage for unloading single face was much greater than that when unloading double faces. Moreover, when double faces were unloaded, the specimen released more strain energy, capable

Table 4 Strain energy density of the two types of strain burst in the σ_1 direction

Type	Total energy density (mJ/mm ³)	Percentage of parts to total strain energy (%)				
		U_d^p	U_d^l	U_e^r	U_d^2	U_r
Unloading single face	1.69	19.3	24.1	17.1	38.4	1.1
Unloading double faces	1.75	3.7	35.1	29.8	28.2	3.2

**Fig. 9** Ejection failure process of strain burst; **a** unloading single face, **b** Face 1 and **c** Face 3 when unloading double faces

of partly transferring to the ejection fragments as kinetic energy.

3.3 Characteristics of Ejection Velocity Field

Figure 9 shows that the ejection was observed in both the strain burst situations. In general, the ejection intensity of a specimen when unloading double faces was stronger than that when unloading single face. Phenomena such as grain ejection, splitting and falling, and fragment ejection all occurred during both types of strain burst tests; however, bending of the rock block in the free faces was observed only when double faces were unloaded. After the burst, a burst

pit was observed on the surface. Additionally, the depth of burst pit (as listed in Table 5) for unloading single face was larger than the depth for unloading double faces.

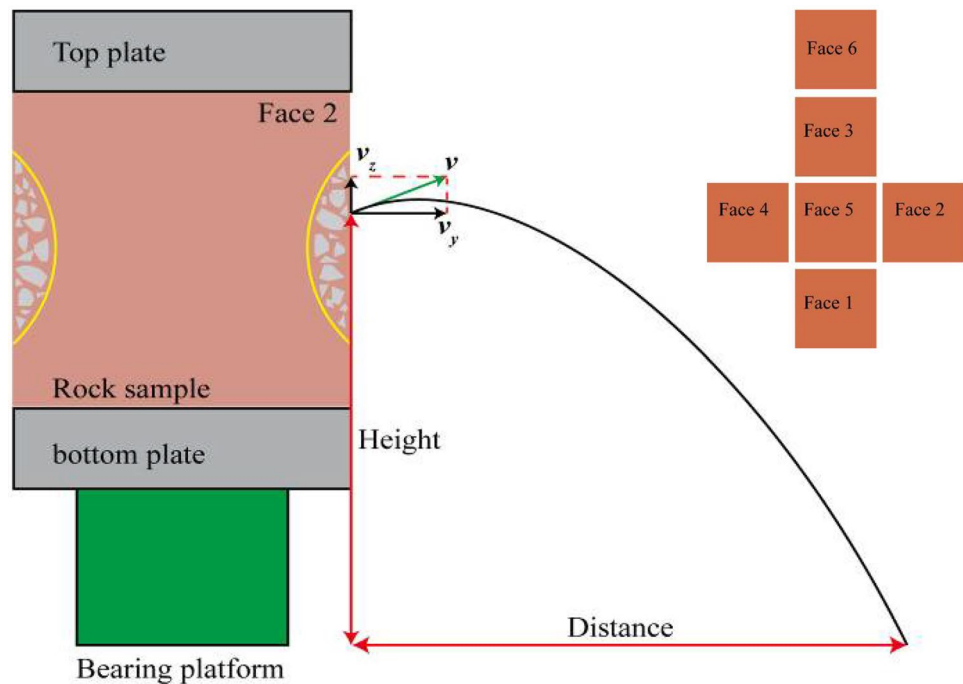
In order to obtain the ejection velocity field of fragments, particle image velocity (PIV) was used to analyze fragment ejection. PIV technique (Meinhart et al. 1999) is typically used to measure the velocity field of a fluid because tracer particles can be easily added to fluids. The minerals in a rock can also be detected and tracked using the camera, thus easily allowing the PIV technique to be used to determine the initial ejection velocity of fragments.

Figure 10 shows the ejection model of fragments. The velocity (v) of ejection fragment can be resolved into the

Table 5 Failure information of the two types of strain burst

Type	Dimension of burst pit (mm)		Maximum initial ejection velocity (m/s)	Maximum kinetic energy (J)	$(U_d)_{max}/U_e^r(\%)$	Total length of cracks (mm)		
						Shear	Buckling	Splitting
Unloading single face	100.4×92.5×18.6		0.75	0.032	3.3×10^{-3}	160.8	510.6	1121.3
Unloading double faces	Face 1	150.5×149.8×16.7	3.75	3.58	0.21	448.9	457.1	740.1
	Face 3	98.7×74.9×7.5	1.25	0.097				

Fig. 10 Schematic of ejection model of the strain burst fragments (After He et al. 2012b)



horizontal (v_y) and vertical (v_z) components. However, during the shooting, the high-speed camera was positioned at a certain angle to the surface of sample. When unloading single face (Fig. 3e), the angle between the visual plane of camera and horizontal axis was 19.9° . In contrast, when double faces were unloaded (Fig. 3f), both the angles between the visual plane of two high-speed cameras and the axis of minimal principal stress were 38.5° . Therefore, the horizontal component of ejection velocity was corrected by dividing the cosine values of the corresponding angles.

In this study, single camera was not perpendicular to the specimen surface, which resulted in errors. Moreover, error analysis should be conducted by setting different types of angles. However, the main objective of this research was to compare the commonalities and differences between strain bursts when unloading single and double faces. The PIV analysis was carried out under the same relative error; thus, the absolute error of ejection velocity was not estimated.

To describe the variation of velocity, a rectangular zone (as shown in Fig. 11a) was selected on the free face to show the variation of statistical mean velocity during the entire ejection. Figure 11a shows the curve of mean velocity of rectangular statistical area, revealing that the mean velocity of free face first increases and then decreases, regenerates, and then decreases once again. The burst process can be divided into the following four sections: I—splitting stage, II—spalling stage, III—early stage of fragment ejection, and IV—late stage of fragment ejection. The early stage of fragment ejection starts from the start of fragment ejection until the debris leaves the parent block, whereas the late stage starts when the fragments leave the parent block. When splitting occurs, the mean velocity increases gradually. The initial ejection velocity was determined according to the spalling action. Moreover, the maximum ejection distance was determined according to the maximum initial ejection velocity. Thus, point B of stage II was selected to obtain

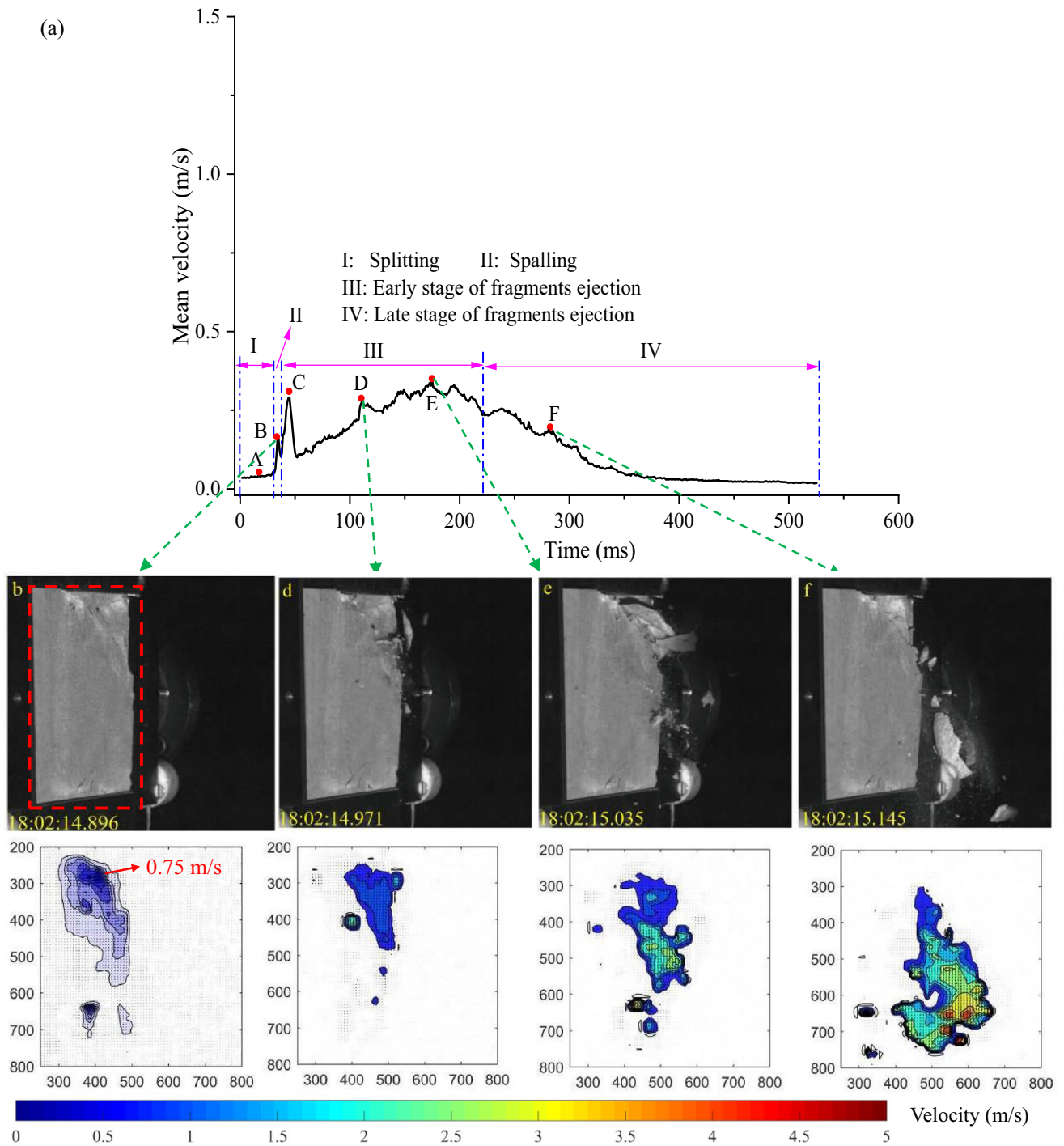


Fig. 11 Variation of the mean velocity of the free face during the ejection failure process and the ejection photographs and corresponding velocity field of typical points (B, D–F); **a** unloading single face, **b** Face 1 and **c** Face 3 when unloading double faces

the maximum initial ejection velocity because the fragments accelerated dropping due to gravity after stage II.

Figure 11a also shows the high-speed photographs and the corresponding velocity vector field of some typical points. During stage I (splitting), local velocities increased; however, during stage II (spalling), the

velocities of specimen surface increased, in particular, in the top right corner. The maximum ejection velocity was 0.75 m s^{-1} . Therefore, the maximum initial kinetic energy of a fragment obtained from the parent could be calculated if the mass of fragment was measured. During the fragment ejection (stages III and IV), the direction

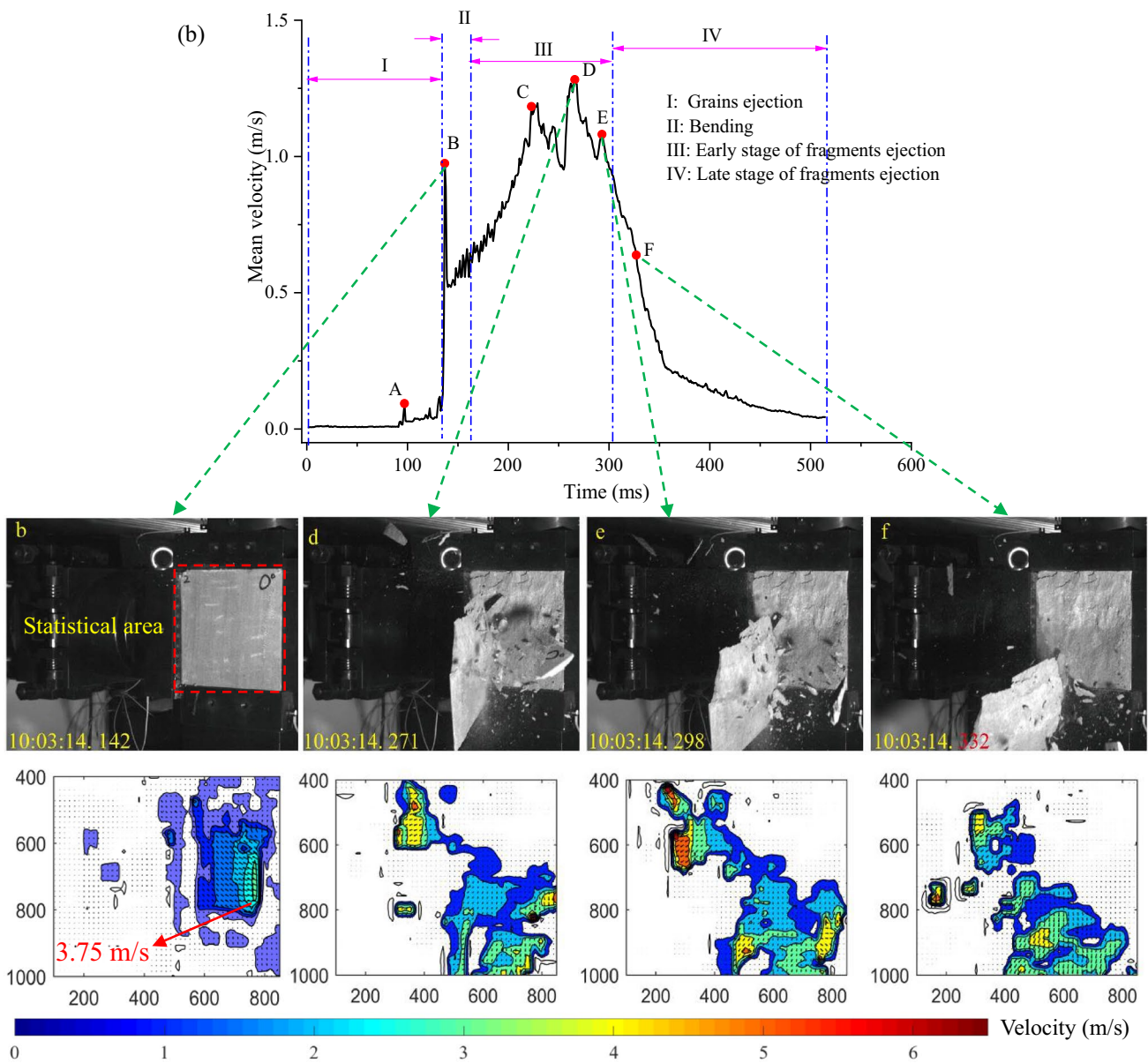


Fig. 11 (continued)

of velocity vector field at the beginning was horizontal (point C) and gradually changed to vertical (point F) due to gravity. Moreover, the maximum velocity of fragments was 5 m s^{-1} at the bottom of ejection fragments.

Figure 11b, c shows the variation in the mean velocity and ejection velocity field of two free faces (Faces 1 and 3) for the unloading of double faces. Whether one or two free faces, the evolution of mean velocity was similar that suddenly increases first and then decreases, then the gradient increases to the extremum value and then decreases to zero. However, when unloading double faces, the increment in the amplitude of mean velocity of Face 1 was greater in the splitting stage than that when unloading single face. In

general, the values of mean velocity of Face 1 during strain burst when unloading double faces were greater than those of free face during strain burst when unloading single face. Moreover, the high-speed photographs of typical points show that bending occurs in the stronger strain burst.

For one free face (Face 1), the direction of grain ejection was horizontal, and the velocity was about 1 m s^{-1} . The direction of bending block velocity was oblique upward, and the maximum velocity was 3.75 m s^{-1} located in the right border of block. However, during fragment ejection, the maximum ejection velocity was 6.5 m s^{-1} in an oblique downward direction. For another free face (Face 3), the mean velocity of Face 3 was less than that of Face 1, and the ejection area was in

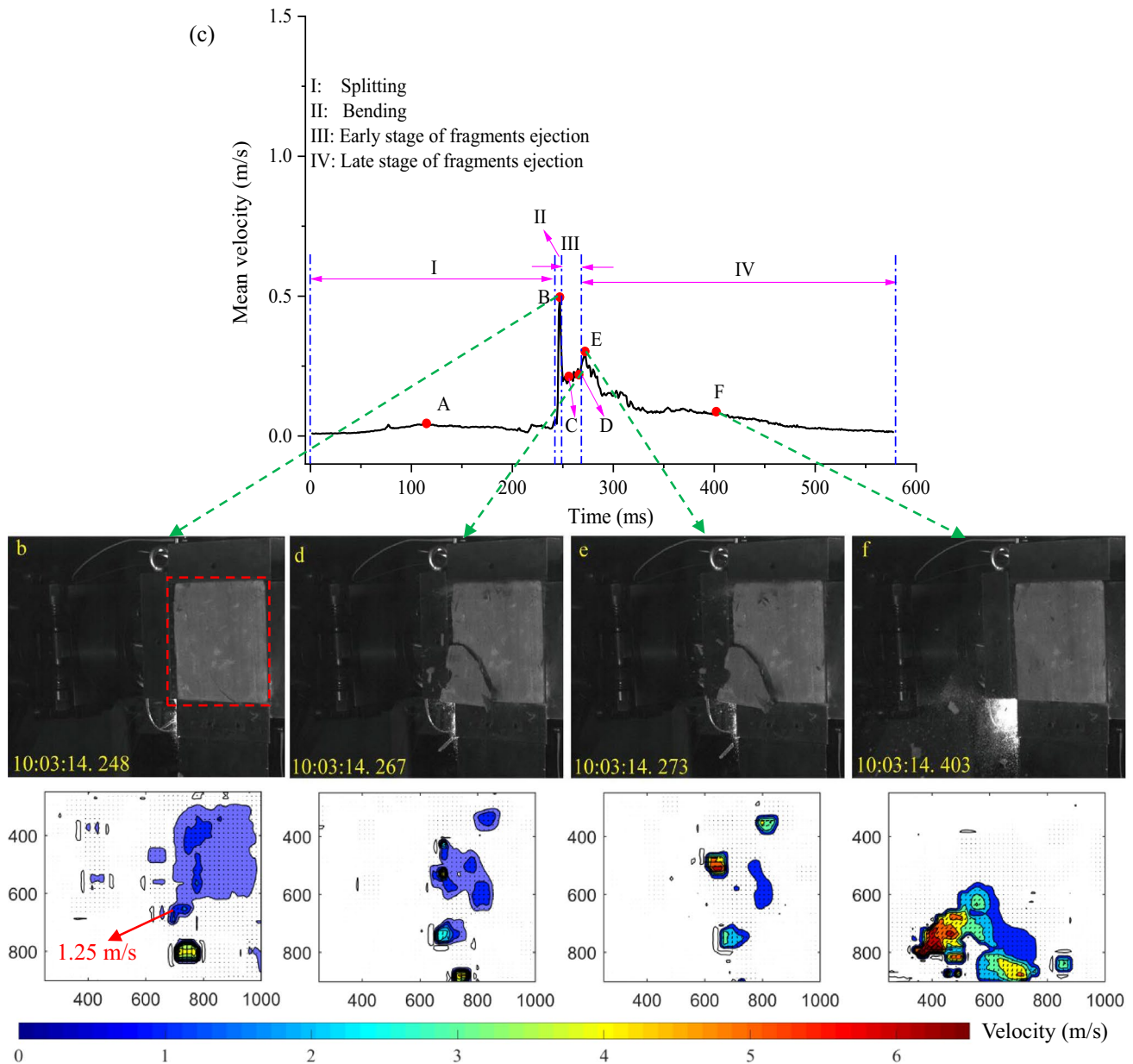


Fig. 11 (continued)

the bottom left corner, which was also smaller. When bending occurred (B point), the maximum ejection velocity was 1.25 m s^{-1} for a point located in the bottom left corner of ejection block. According to the maximum initial ejection velocity, the maximum kinetic energy of ejection fragments can be estimated using Eq. (5) as follows:

$$(U_k)_{\max} = \frac{1}{2} m v_{\max}^2, \quad (5)$$

where U_k is the kinetic energy, m is the total mass of ejection fragments, and v_{\max} is the maximum initial ejection velocity.

Table 5 presents the maximum kinetic energy of two types of strain burst and the ratio of kinetic energy to releasable elastic energy (U_e^r). When double faces were unloaded, more energy (0.21%) was transferred to kinetic energy compared to the situation when single face unloading was carried out ($3.3 \times 10^{-3}\%$). Moreover, the maximum kinetic energy of unloading single face was smaller than that for unloading double faces.

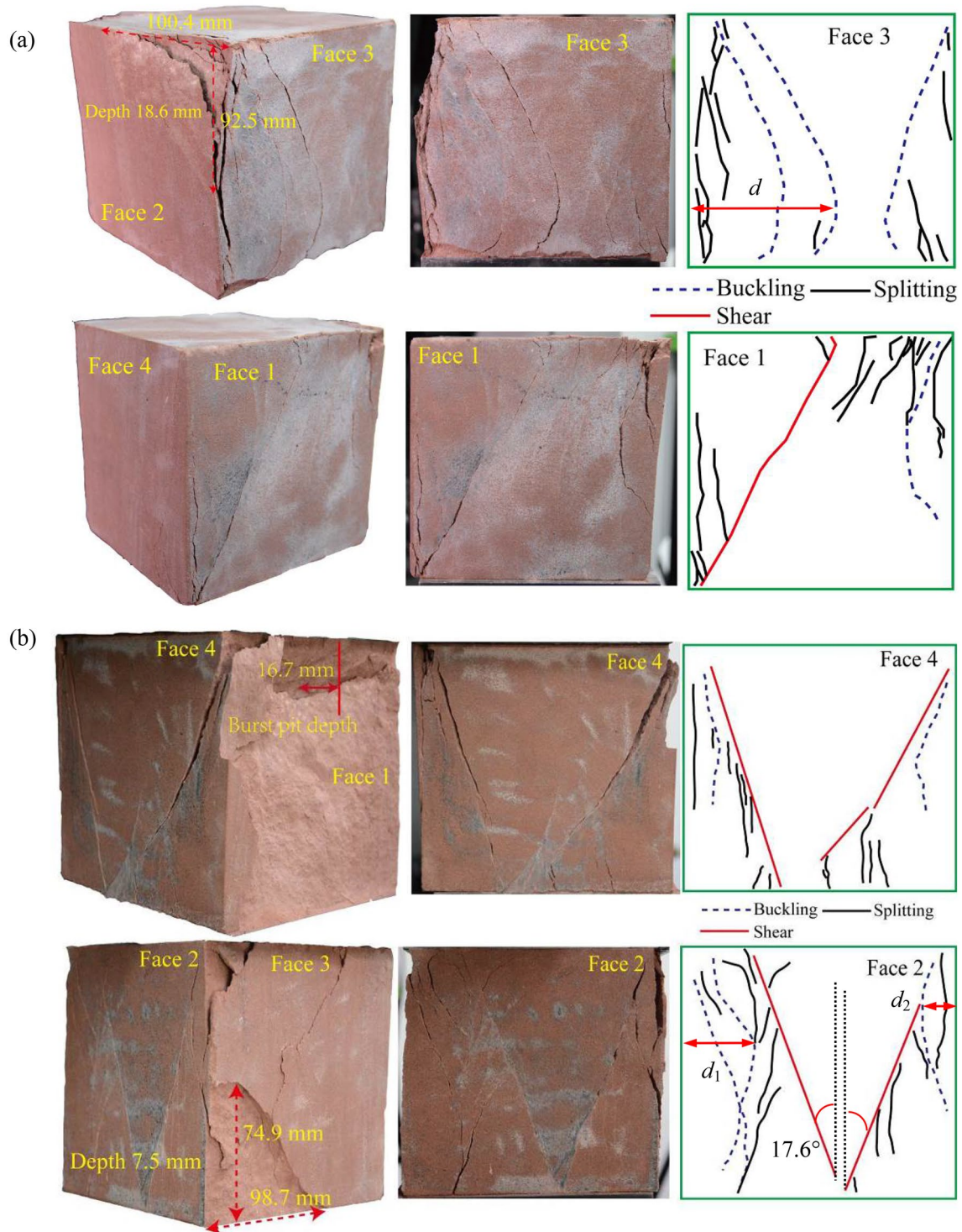


Fig. 12 Failure photographs and sketch maps of the surface cracks for the two types of strain burst; unloading **a** single and **b** double faces

3.4 Failure Modes

Figure 12 shows the photographs of failure modes corresponding to two types of strain burst (unloading of single and double faces) and the corresponding sketch maps of

surface cracks. When unloading single face, three obvious buckling cracks were observed in Face 3, and the ratio of maximum distance (d , as shown in Fig. 12a) between a buckling crack and the free face to the height was 0.58. Several splitting cracks with intersection angles with the

free face of less than 10° were found to be formed on Face 3. In the opposite face (Face 1), a shear crack from top to bottom was formed with an intersection angle and with a vertical axis of 29.4° . Furthermore, several tensile cracks (splitting) surrounded the shear crack. The splitting and buckling cracks were concentrated at the top right corner, close to the free face of specimen. Table 5 lists the total length (the curve simplified to multiline segments) of shear, buckling, and splitting cracks.

Figure 12b demonstrates that when unloading double faces, the breakthrough of shear cracks occurred along the width of rock sample, and two shear fracture zones occurred. Moreover, the fracture angle of the two shear cracks on Face 2 was 17.6° . Similarly, tensile cracks (splitting) also accompanied the shear cracks. Furthermore, buckling cracks also occurred near the shear fracture zone, and the ratios of maximum distances (d_1 and d_2) between the buckling cracks and free face to the height of specimen for Faces 1 and 3 were 0.27 and 0.12, respectively. Moreover, the splitting cracks close to the free face were approximately parallel to the free face. Table 5 summarizes that the total length of surface shear cracks when unloading double faces was ~ 2.8 times greater than that when unloading single face. However, when unloading single face, the specimen shows a greater length of surface buckling and splitting cracks (both tensile cracks).

In general, whether single or double faces were unloaded, four typical fracture subregions (shear, buckling, splitting, and ejection zones) were observed on the specimen surface in the direction of intermediate principal stress, and Fig. 13 exhibits the evolution process of the four subregions. The shear and tensile microcracks developed during the loading, especially the slabbing phenomenon was occurring near the free face. Additionally, when the specimen yielded, tensile microcracks broke to form the buckling and splitting zones. Moreover, when burst occurred, the shear fracture zone was gradually shaped by the coalescence of shear microcracks.

Concurrently, a small part of releasable elastic energy was transferred into kinetic energy and formed an ejection zone in the free face.

After burst, the ejection fragments of two types of strain burst were collected and screened using standard sieves (with five ranges of diameter). The particle diameter was defined as the maximum length of any two points of fragment. Moreover, the fragment dimensions (length, width, and thickness all exhibited the maximum values in three directions) were measured to show the shape of fragments. Figure 14a, b shows that the second type of strain burst (unloading double faces) exhibited more fragments with diameters greater than 10 mm. Figure 14c shows the distribution of mass percentage of the five fragment groups with different particle diameters. For the two types of strain burst, most of the mass was distributed in fragments with diameters greater than 10 mm.

Figure 14e, f shows the distribution histogram of fragments with different ratios—length (l) to thickness (h), length to width (w), and width to thickness based on the measured dimensions of ejected fragments. When unloading only single face, the ratios of length to thickness, length to width, and width to thickness were in the range from 4.13 to 11.77, 1.11 to 4.27, and 1.1 to 7.79, respectively. In contrast, when double faces were unloaded, the three ranges were, respectively, 3.49 to 15.7, 0.98 to 3.2, and 1.9 to 8.18. Moreover, Fig. 14e, f also shows the fitting probability density function. Both strain burst experiments exhibited normal or lognormal distributions, and the mean values of each distribution are marked in the figures. The ratios of length to thickness and width to thickness represent the flaky feature; and the ratio of length to width was used to indicate if a particle was massive (larger l/h , w/h corresponding to more obvious flaky feature and smaller l/w corresponding to more obvious massive feature). The ratios (l/h , w/h) of fragment sizes when unloading double faces were greater than those

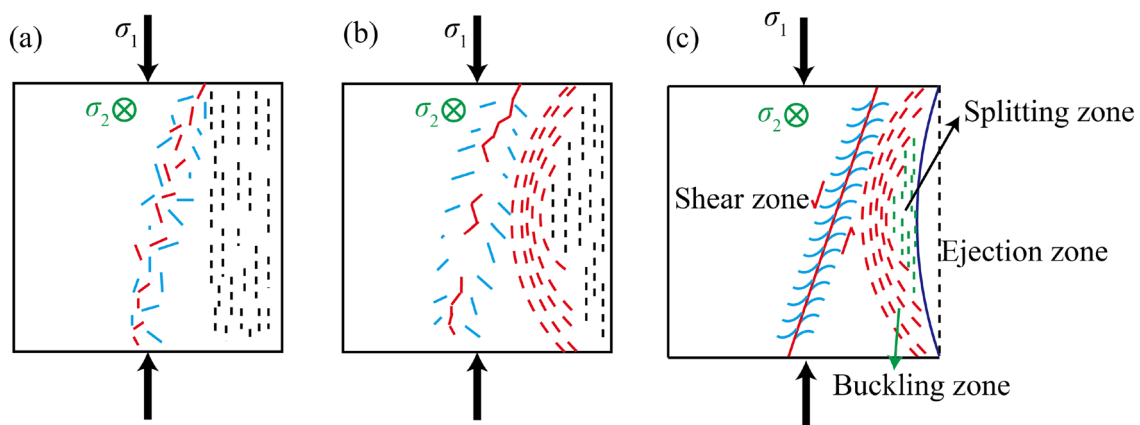


Fig. 13 Evolution process of subregions of strain burst fracture; **a** slabbing, **b** buckling and **c** shear cracks penetration and fragments ejection

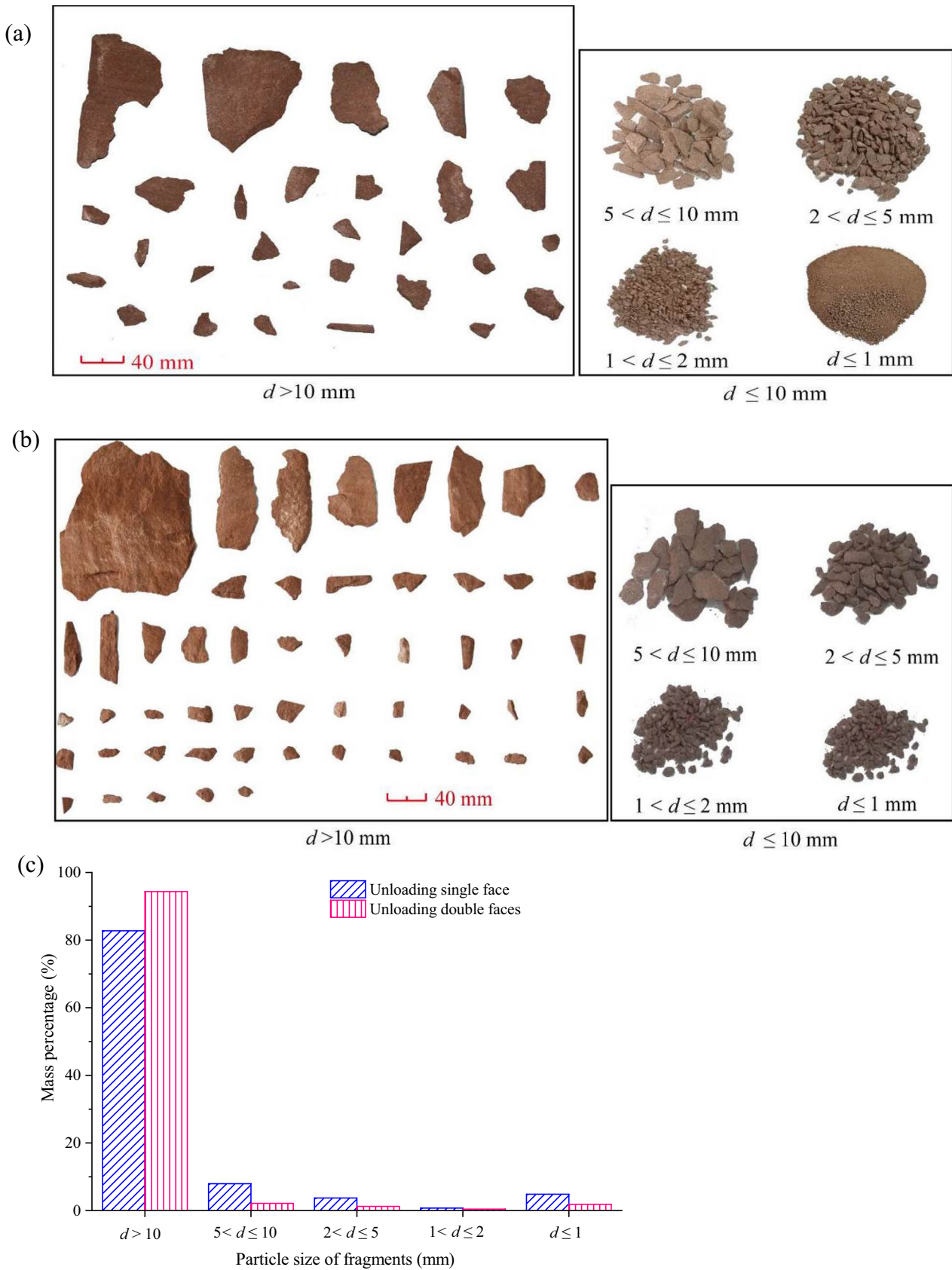


Fig. 14 Photographs of ejection fragments with different particle diameters for the two types of strain burst; unloading **a** single and **b** double faces; **c** distribution of mass percentage of fragments; distribution characteristics of fragments size; unloading **e** single and **f** double faces

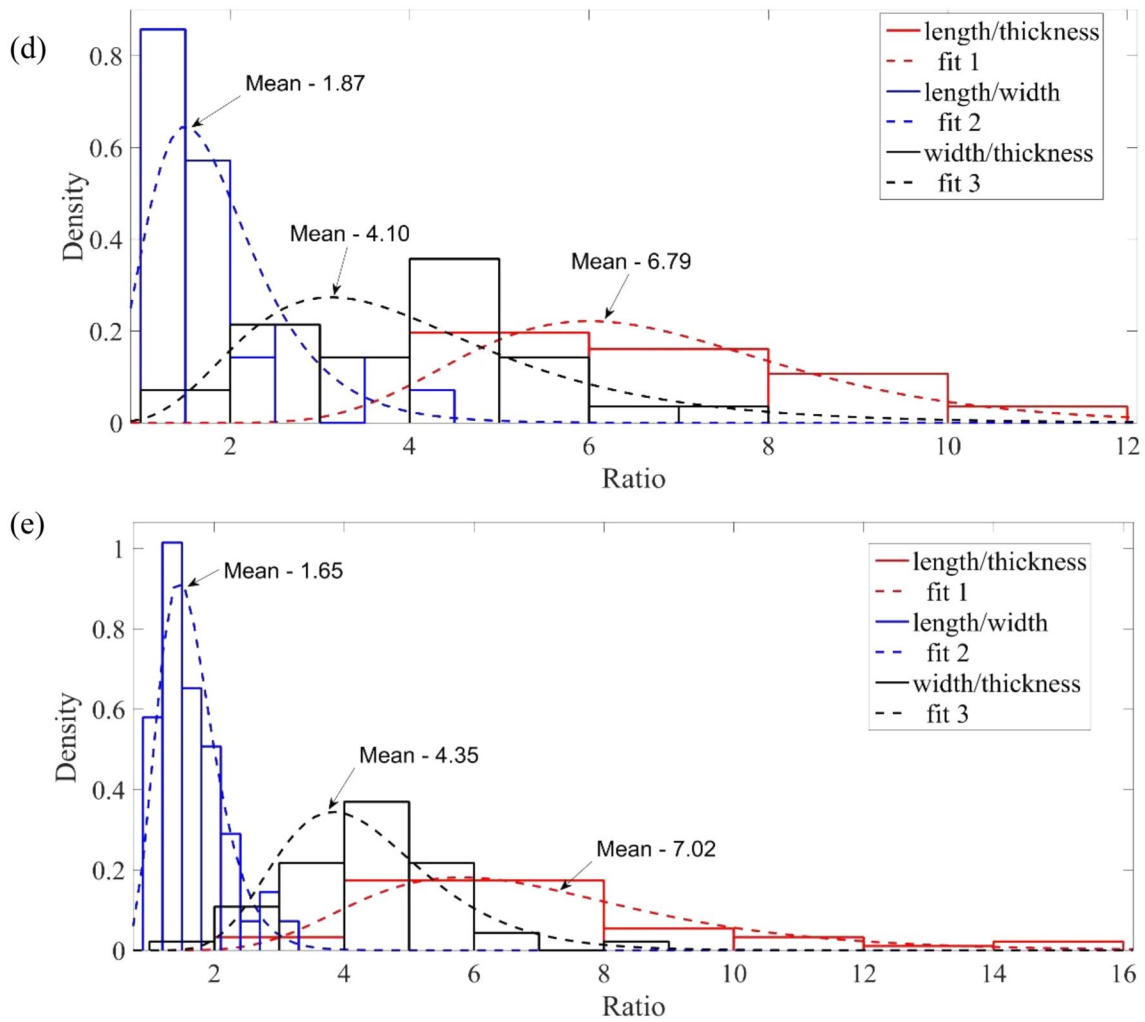


Fig. 14 (continued)

when unloading single face; however, the ratio of length to width was opposite. When strain burst occurred, while unloading double faces, both flaky and massive features were obvious for fragments ejected from the block.

3.5 Acoustic Emission Characteristics

Figure 15 demonstrates that the AE counts and accumulated energy indicate AE activity and the energy release, respectively. The loading processes of the two types of strain burst were divided into the following five stages: Stage I was the initial loading stage; stage II_1 was the unloading stage (from the start of unloading to exposing the free face completely); stage II_2 was the continuous deformation stage; stage III was the yielding stage; and stage IV was the burst stage.

In stage I, AE activities for the two types of strain bursts were both weak; however, during the unloading (stage II_1), both the AE activities exhibited a sudden increase. During

the continuous deformation stage (II_2), strong AE activities were frequent. Subsequently, when unloading double faces (Fig. 15c), AE activities were concentrated toward the end of stage II_2 . AE activity of the two types of strain burst showed sustainable strong activity during the yielding stage (III). However, the intensity of AE activity began to decrease during the burst stage for strain burst during the unloading of single face, whereas strong AE activities lasted from yielding point to the end of burst when unloading double faces. Moreover, most of the accumulated energy of AE occurred during the yielding stage; however, the burst stage showed a slight increase.

The peak frequency of AE signal was used to evaluate the microcrack size. A larger microcrack corresponds to an AE signal with a smaller peak frequency, and vice versa (Grosse and Ohtsu 2008). Figure 16 shows the variation in peak frequency and amplitude of AE signals during the two types of strain burst. For strain burst during the unloading of single

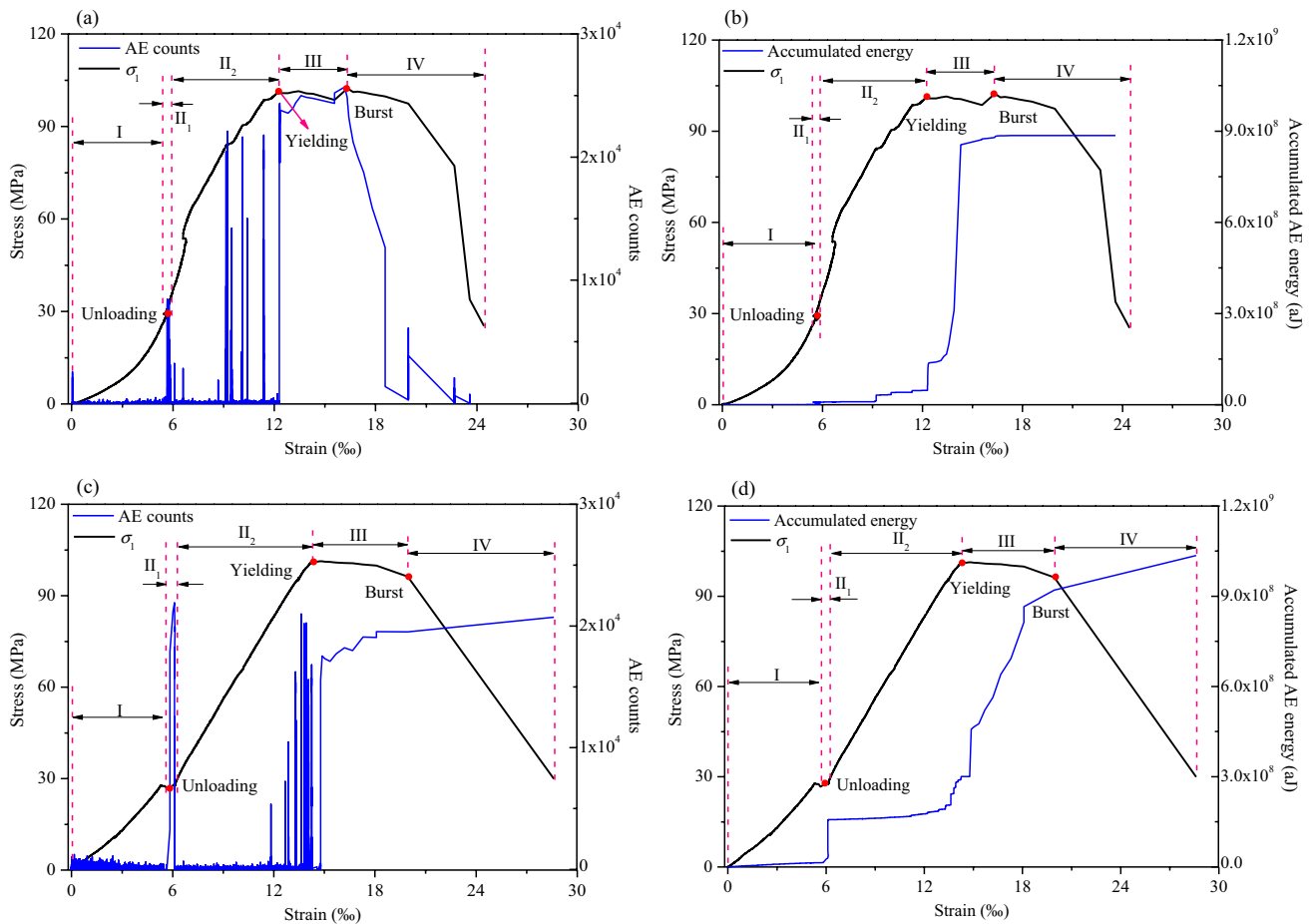


Fig. 15 Variation of AE counts (a and c) and accumulated energy (b and d) of two types of strain burst; a and b unloading single face, c and d unloading double faces

face, most of the AE signals occurred before the yielding of specimen (Fig. 16a), and the peak frequencies were in the range from 100 to 520 kHz. However, the peak AE signal frequencies occurring from yield to burst ranged from 200 to 250 kHz. Furthermore, their amplitudes were both greater than 70 dB. During the burst stage, the amplitudes of AE signal were less than 70 dB, with peak frequency ranging from 180 to 280 kHz.

Figure 16b illustrates that for strain burst that occurred while unloading double faces, the peak frequencies of the AE signals from initial to the yielding point ranged from 120 to 430 kHz. After yielding, the peak frequencies ranged from 138 to 155 kHz, and all the amplitudes were greater than 80 dB. Therefore, AE signals that occurred during the burst when unloading double faces exhibited a lower frequency, i.e., the microcracks were larger than that for unloading single face.

Additionally, the “relative quiet period” (from yield to burst) could be observed from Fig. 16, and similar results had been reported in the literature (Hu et al. 2019). However, there was no systematic understanding of the reason of the

quiet period. In our opinion, before the yield point, there were many microcracks in the specimen. On the one hand, the microcracks changed the internal stress field of the rock and a new balance was needed before further propagation and penetration; on the other hand, the microcracks reduced the integrity of rock, making it difficult to transmit the elastic wave formed by microcracks. Hence, only a few signals with high amplitude and low frequency were received.

Notably, the types of microcracks were classified according to the average frequency (AF) and RA (rise time/amplitude, unit: ms v^{-1}) value of AE signal (Grosse and Ohtsu 2008). Figure 17a shows the schematic illustration of the method to classify microcracks based on the scatters of AF–RA. A boundary line with slope k divides the coordinate system into two parts: The upper part is a tensile crack, whereas the lower section is a shear crack. Linear discriminant analysis (LDA) was performed on the AE data (RA, AF) of the three-point bending and direct shear tests. The determined critical slope (1.21) is shown in Fig. 17b, and Fig. 17c shows the confusion matrix of LDA. In general, about 91.8% of the AE data could be correctly classified.

Fig. 16 The peak frequency and amplitude variation during the two types of strain burst; unloading (a) single and (b) double faces

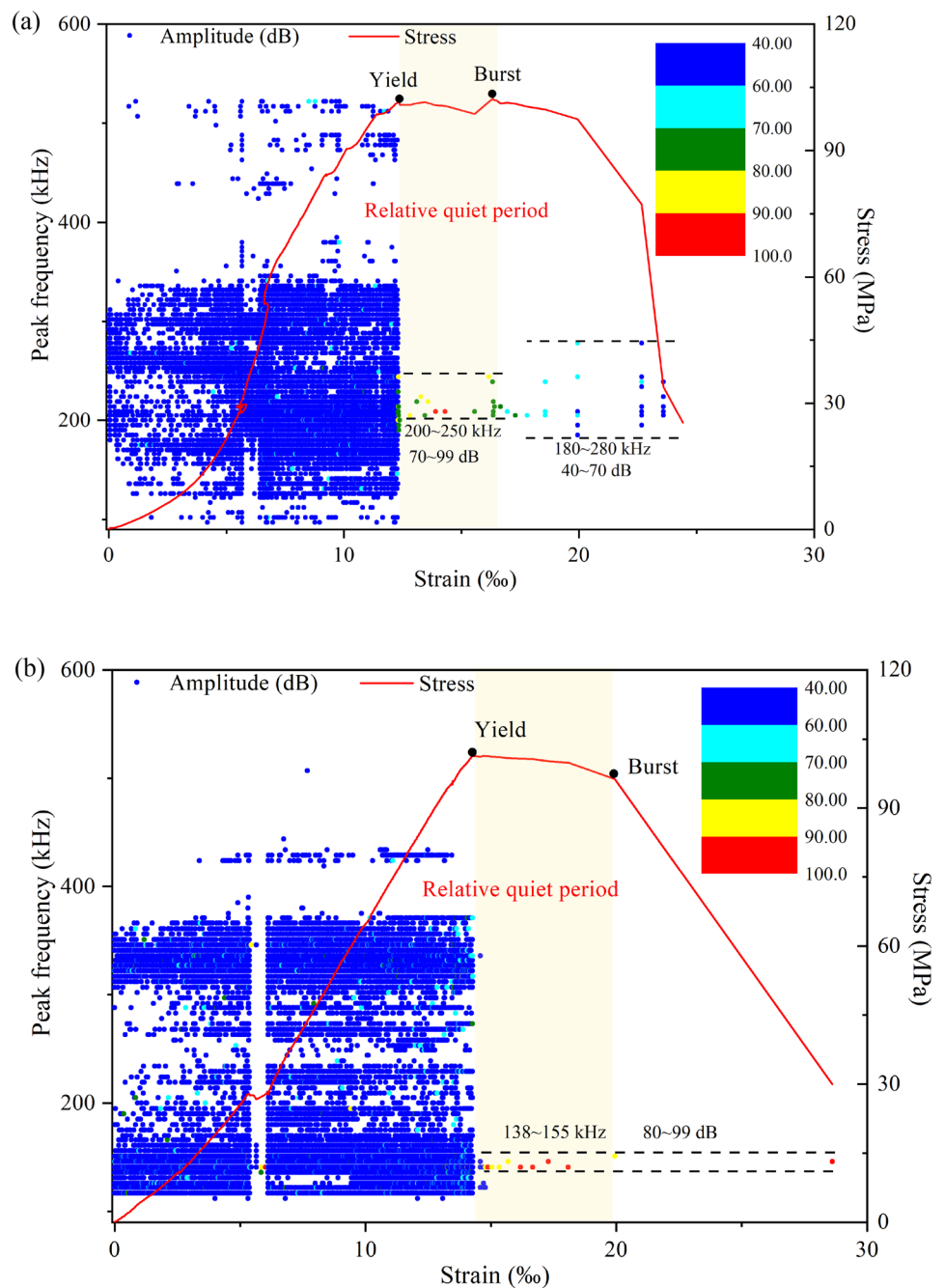


Figure 17d, e exhibits the variation in the scatters of AF-RA in the five stages (as shown in Fig. 17) when single and double faces were unloaded, respectively. The numbers in the figure indicate the ratios of tensile to total microcracks. In general, the changes in the ratio of the two types of strain burst were similar. In stage I, the numbers of shear and tensile microcracks were approximately equal; and the percentage of shear microcracks increased due to unloading during both types of strain burst tests. Moreover, when double faces were unloaded, the increment in shear microcrack percentage was greater than that when unloading single

face. In the continuous deformation stage (II₂), the numbers of shear and tensile microcracks were also similar for the strain burst when unloading single face, while tensile microcracks were greater than shear microcracks by about 7% for unloading double faces. During stages III and IV, the shear microcracks dominated for the two types of strain burst. Furthermore, from yield to burst, the percentage of tensile microcracks for previous strain burst was greater than that for the current stage of strain burst by about 11%. These phenomena also correspond to the total length of surface cracks (as presented in Table 5).

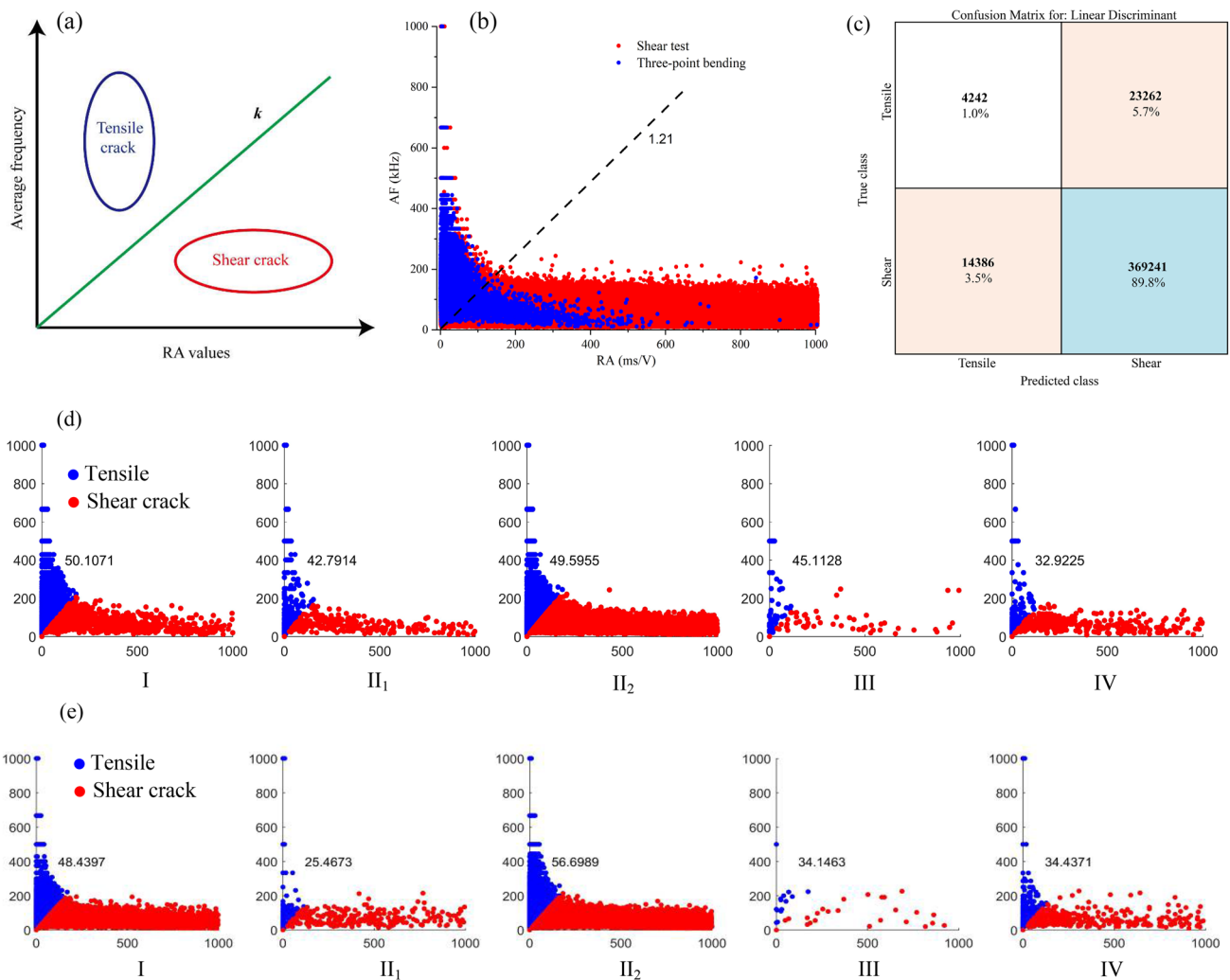


Fig. 17 **a** Schematic of crack type classification with a combination of average frequency and RA values (Grosse 2008); **b** linear classification boundary of AF–RA from shear and three-point bending tests; **c** confusion matrix of linear discriminant analysis; variation of

the proportions of tensile and shear microcracks at different stages for unloading **d** single and **e** double faces (the numbers in the figures are the ratio of tensile to total microcracks in each stage)

4 Conclusion

In this study, a new strain burst experimental system was used to perform two types of strain burst tests by rapidly unloading single and double faces (in one direction), to simulate the strain burst occurring in surrounding rock of tunnel or double tunnel faces during the opposite tunneling. A high-speed image recording system and AE system monitored the failure process of strain burst when single or double faces were rapidly unloaded. The commonalities and differences between the abovementioned two types of strain burst were analyzed from five aspects: Failure stress, strain energy dissipation, ejection velocity field, failure modes, and AE characteristics. The specific conclusions are as follows:

(1) The failure stress and percentage of dissipation energy due to crack propagation were approximately equal for two

types of tests. Moreover, the evolution of mean velocity of free face was similar that suddenly increased first and then decreased, and then the gradient increased to the extremum value and finally decreased to zero. Further, the failure sub-regions of the fracture were consistent in that both contained shear, buckling, splitting, and ejection zones.

(2) The strain burst intensity when unloading double faces was greater than when unloading single face. This greater intensity is manifested in the larger initial ejection velocity, larger volume of burst pit, and lower peak frequency. Furthermore, during strain burst when unloading double faces, both the flaky and massive fragments were more obvious than when unloading single face. Moreover, from yield to burst, strain burst when unloading double faces contained more shear microcracks, whereas strain

burst when unloading single face showed more tensile microcracks.

Acknowledgements Financial support from the National Key Research and Development Program (Grant no. 2016YFC0600900), National Natural Science Foundation of China (Grant no. 41941018 & 52074299) and Province Education Department of LiaoNing (Grant no. 2020LNQN04) are gratefully acknowledged.

Compliance with Ethical Standards

Conflict of interest The authors declared that there is no conflict of interest to this work.

References

- Akdag S, Karakus M, Taheri A et al (2018) Effects of thermal damage on strain burst mechanism for brittle rocks under true-triaxial loading conditions. *Rock Mech Rock Eng* 51(6):1657–1682
- Alexeev A, Revva V, Alyshev N et al (2004) True triaxial loading apparatus and its application to coal outburst prediction. *Int J Coal Geol* 58(4):245–250
- Cai M, Kaiser P (2018) Rockburst support reference book—volume 1: rockburst phenomenon and support characteristics. Laurentian University, Mirarco
- Chang S, Lee C (2004) Estimation of cracking and damage mechanisms in rock under triaxial compression by moment tensor analysis of acoustic emission. *Int J Rock Mech Min Sci* 41(7):1069–1086
- Chen B, Feng X, Li Q et al (2015) Rock burst intensity classification based on the radiated energy with damage intensity at Jinping II hydropower station. *China Rock Mech Rock Eng* 48(1):289–303
- Feng X, Zhao J, Zhang X et al (2018) A novel true triaxial apparatus for studying the time-dependent behaviour of hard rocks under high stress. *Rock Mech Rock Eng* 51(9):2653–2667
- Grosse C, Ohtsu M (2008) Acoustic emission testing. Springer, Berlin Heidelberg
- He M, Miao J, Feng J (2010) Rock burst process of limestone and its acoustic emission characteristics under true-triaxial unloading conditions. *Int J Rock Mech Min Sci* 47(2):286–298
- He M, Xia H, Jia X et al (2012) Studies on classification, criteria and control of rockbursts. *J Rock Mech Geotech Eng* 4(2):97–114
- He M, Nie W, Guo W (2012) Experimental investigation of bedding plane orientation on the rockburst behavior of sandstone. *Rock Mech Rock Eng* 45(3):311–326
- He N, Ma Q, Shi Y (2012) The optimum arrangement of working face ventilation system for coal mine. *Adv Mater Res* 482–484:1691–1694
- He M, Ren F, Cheng C (2018) Experimental and numerical analyses on the effect of stiffness on bedded sandstone strain burst with varying dip angle. *Bull Eng Geol Env* 78(5):3593–3610
- Hu X, Su G, Chen G et al (2019) Experiment on rockburst process of borehole and its acoustic emission characteristics. *Rock Mech Rock Eng* 52(3):783–802
- Huang D, Li Y (2014) Conversion of strain energy in triaxial unloading tests on marble. *Int J Rock Mech Min Sci* 66(1):160–168
- Kaiser P, McCreath D, Tannant D (1996) Rockburst research handbook. Volume 2: 1990–1995.
- Li J, Li H, Ma G et al (2013) Assessment of underground tunnel stability to adjacent tunnel explosion. *Tunnell Undergr Space Technol Incorp Trench Technol Res* 35:227–234
- Mansurov V (2001) Prediction of rockbursts by analysis of induced seismicity data. *Int J Rock Mech Min Sci* 38(6):893–901
- Meinhart C, Wereley S, Santiago J (1999) PIV measurements of a microchannel flow. *Exp Fluids* 27(5):414–419
- Miao S, Cai M, Guo Q et al (2016) Rock burst prediction based on in-situ stress and energy accumulation theory. *Int J Rock Mech Min Sci* 83:86–94
- Nemat-Nasser S, Horii H (1982) Compression-induced nonplanar crack extension with application to splitting, exfoliation, and rockburst. *J Geophys Res Sol Earth* 87(B8):6805–6821
- Ortlepp W, Stacey T (1994) Rockburst mechanisms in tunnels and shafts. *Tunn Undergr Space Technol* 9(1):59–65
- Plessis M, Malan D (2014) Designing controlled pillar failure—crush pillar support. In: The 6th international platinum conference, ‘platinum—metal for the future’, The Southern African Institute of Mining and Metallurgy.
- Ren F, Zhu C, He M (2020) Moment tensor analysis of acoustic emissions for cracking mechanisms during schist strain burst. *Rock Mech Rock Eng* 53(1):153–170
- Salamon M (1984) Energy considerations in rock mechanics: fundamental results. *J South Afr Inst Min Metall* 84(8):233–246
- Si X, Gong F (2020) Strength-weakening effect and shear-tension failure mode transformation mechanism of rockburst for fine-grained granite under triaxial unloading compression. *Int J Rock Mech Min Sci* 131:104347
- Su G, Chen Z, Ju J et al (2017) Influence of temperature on the strain-burst characteristics of granite under true triaxial loading conditions. *Eng Geol* 222:35–52
- Su G, Jiang J, Zhai S et al (2017) Influence of tunnel axis stress on strainburst: an experimental study. *Rock Mech Rock Eng* 50(6):1551–1567
- Su G, Zhai S, Jiang J et al (2017) Influence of radial stress gradient on strainbursts: an experimental study. *Rock Mech Rock Eng* 50(10):2659–2676
- Sun Y, Tan C (1995) An analysis of present-day regional tectonic stress field and crustal movement trend in China. *J Geomech* 1(3):1–12 ((in Chinese))
- Tesarik D, Seymour J, Yanske T (2009) Long-term stability of a back-filled room-and-pillar test section at the Buick Mine, Missouri, USA. *Int J Rock Mech Min Sci* 46(7):1182–1196

Publisher's Note Springer Nature remains neutral with regard to jurisdictional claims in published maps and institutional affiliations.



Mancho He is a professor of China University of Mining and Technology, Beijing. At present, he is Vice President of International Society for Rock Mechanics. His research interests contain rockburst mechanism, mining technologies, active fault stability analysis. He has undertaken several research projects as a leader, related to the geomaterial properties and the stability of geotechnical engineering in deep ground. He has obtained one National Prize for Inventions of China and two National Prizes

for Progress in Science and Technology of China. He has published 4 books and more than 200 articles.



Fuqiang Ren received the B.S degree in civil engineering from the Institute of Disaster Prevention, Langfang, China, in 2014, and the PhD. Degree in geotechnical engineering from China University of Mining and Technology, Beijing, China, in 2019. At present, he is a lecturer of University of Science and Technology LiaoNing. His research interest includes rock mechanics and geological disaster evaluation. He has published over 20 articles in related international conference proceedings and

journals. He is the holder of 3 patents.



Shudong Zhang received the B.S degree in civil engineering from the North China Institute of Aerospace Engineering, Langfang, China, in 2018. At present, he is a master student of China University of Mining and Technology, Beijing. His research interest is rock mechanics.



Dongqiao Liu received the PhD. Degree in geotechnical engineering from China University of Mining and Technology, Beijing, China, in 2014. At present, he is an associate professor of China University of Mining and Technology, Beijing. He has undertaken three research projects as a leader, related to the rock mechanics. Her research interest includes rock damage mechanics, rockburst mechanism and disaster prevention. He has published over 20 articles, and he is the holder of 5 patents.